Pharmaceutical Research, Vol. 23, No. 10, October 2006 (© 2006)
DOI: 10.1007/s11095-006-9073-7

Research Paper

Modeling of Aqueous Transport in Rigid Porous Matrices near the Percolation Threshold

Scott R. Ellis[1,3] and James L. Wright[2]

Received January 18, 2006; accepted May 22, 2006; published online August 24, 2006

Purpose. To demonstrate control of passive diffusion of small molecules through rigid ceramic matrices via manipulation of matrix porosity near the percolation threshold, and to model such control using percolation scaling relationships on both infinite and finite lattices.
Materials and Methods. Rigid alumina disks of controlled porosity were prepared using standard ceramic casting and sintering techniques. Structural void space distributions in sintered disks were measured by dimensional and volume displacement (pycnometry) methods. The impact of void space on transport was determined by tracking the diffusion of ionized benzoic acid across sintered disks mounted in Stokes diffusion cells. Critical percolation thresholds were estimated by fitting structural and transport-dependent results to percolation scaling relationships. Finite-size scaling studies were performed by adding polymer microspheres of known diameter to the disks to generate artificially large pores.
Results. Nonlinear least squares techniques were used to fit both structural and transport-dependent properties of rigid alumina disks to total disk porosity using percolation scaling relationships. The critical percolation threshold determined from structural properties (0.129) was lower than that determined from benzoic acid transport (0.169). The transport-derived percolation threshold exactly matched that expected for a tetrakaidecahedral (14 sided) lattice. Finite-size scaling was demonstrated through a nonzero effective volume fraction for transport at the percolation threshold.
Conclusions. Manipulation of total disk porosity near the percolation threshold was shown to be a suitable means of controlling the transport rate of a model small molecule, while deliberate enlargement of individual pores was demonstrated to decrease this threshold without increasing total porosity. The lower-than-expected percolation threshold obtained from the structural model was ascribed to limitations of the measurement technique. The threshold determined from the aqueous transport model was concluded to represent the true threshold for this system.

KEY WORDS: alumina; finite-size scaling; percolation; tetrakaidecahedron; transport.

INTRODUCTION

Alumina (aluminum oxide, Al_2O_3), a common ceramic biomaterial, was evaluated for its potential use as a rigid, porous sustained release carrier for drugs of small molecular dimension (1). It was thought that control of passive diffusion in such a device could be effected through manipulation of its total porosity ($\varnothing$) near the critical percolation threshold ($\varnothing_c$), a point at which $\varnothing$ becomes large enough such that at least one pore cluster completely spans the device and enables transport across that device (2). Device porosity and its influence on various bulk properties such as transport could then be modeled using percolation theory.

To demonstrate through experiment how percolation theory might be used to model transport near $\varnothing_c$, small Al_2O_3 disks were manufactured using standard ceramic processing methods (3) and their porosity distributions characterized using dimensional and volume displacement techniques. Porosity-dependent resistance to transport was determined by measuring passive diffusion of a model small molecule (ionized benzoic acid) across disks mounted in Stokes diffusion cells (4). Values of $\varnothing_c$ were estimated for both the structural and transport-dependent cases by fitting observed porosity distributions and diffusivities to $\varnothing$ using percolation theory scaling relationships, and used to develop a picture of the overall pore structure and its impact on transport.

The power-law scaling relationships for $\varnothing$ and $\varnothing_c$ represent the particular case of systems of infinite size. For systems that cannot be considered infinite, a technique known as finite-size scaling (5–7) may be applied to describe the impact of size on transport near $\varnothing_c$. The theory of finite-size scaling provides the basis for the existence of scaling in infinite systems, and defines the approach to power-law scaling in the limit of infinite size. Finite-size scaling also provides a means of extracting necessary information for the power law in infinite systems from information and data obtained for finite

[1] Nektar Therapeutics, 150 Industrial Road, San Carlos, California 94070, USA.
[2] Infinity Pharmaceuticals, Cambridge, Massachusetts 02139, USA.
[3] To whom correspondence should be addressed. (e-mail: sellis@nektar.com)

systems. In the present case, the ability to maintain transport of the model small molecule across disks below $\varnothing_c$ may be demonstrated by reducing resistance of individual pores to transport. Finite-size scaling relationships suggested in the literature were verified through experiment in order to illustrate the potential use of this case in transport control.

This paper describes the procedures used to obtain various descriptors of alumina disk porosity for both infinite and finite lattices, and the results of nonlinear least squares fits of these descriptors to percolation theory models. Particular details regarding the study of disk fabrication methods through which porosities were manipulated are not included for sake of brevity.

Applications of percolation theory in pharmaceutical and other industries are manifold, with the method being used to predict behavior of disordered systems in areas as diverse as separations processing (8,9), water vapor transport (10), tablet granulation and compression (11–15), and release control in different drug delivery systems (16–18). While this list is by no means intended as an exhaustive review of the field, these references speak to the power of the method in characterizing and predicting certain behaviors of complex systems through simple measurements of key bulk properties.

Alumina Microstructure and Processing

Alumina is a nonmetallic ionic material that in its thermodynamically stable phase (α-alumina, or corundum) exists as a hexagonal close-packed crystal. The maximum density of this crystal (19) has been reported as 3.98 g/cm^3, which was rounded to 4.0 g/cm^3 for use in this work. Individual groups of alumina crystals, called grains, comprise the broader microstructure along with a random network of voids, or pores, that exist between the grains. The void sizes are assumed to be the same order of magnitude as or larger than the grains themselves. The void network can consist of isolated voids, which are completely surrounded by grains, and accessible voids, which are open to at least one surface of the overall grain/void system. The total void space, or total porosity, is the sum of these two void volumes.

The size and spatial arrangement of the grain structure dictate the shape (tortuosity) and average diameter of the pore network. The arrangement of grains is assumed to be completely random, with the void space around the grains being extremely tortuous. The overall structure of this pore space may be described using a so-called nodes–links–blobs model (20), where the nodes are pore junctions, the blobs are pore bulbs, and the links are pore throats. The mean cross-sectional area of the links in this network controls the rate at which fluid can invade or escape the pore space, but the overall blob volume controls the length of time required to fill or empty this space with fluid. Link and blob radii in a ceramic compact are controlled primarily by the median size and size distribution of Al_2O_3 grains used to form the compact, as well as the mean size and size distribution of the Al_2O_3 bulk powder. Some additional void size and shape control is effected through the manufacturing process. This picture of the microstructure is needed for development of the site percolation model to be considered shortly.

Commercial alumina ceramics are typically made to be as dense as possible to improve strength of the final product (21,22). Eliminating void space by efficient packing of the alumina powder is the most convenient means of reducing final porosity. Small, monodisperse powders and/or powders with small mean diameter and narrow polydispersity are most often used to minimize void space since the highest packing densities may be achieved with such powders. Preserving pore structure and volume were primary concerns of this work, however, and required the use of larger monodisperse and narrowly polydisperse powders in order to reduce packing efficiency and increase total void space in the powder compact.

Manufacture of disk-shaped ceramic compacts in this study consisted of four discrete steps: powder mixing, compaction, pre-firing, and sintering. First, Al_2O_3, magnesium oxide (MgO), and poly(vinylpyrrolidone) (PVP) powders were slurried, mixed, dried, and milled to generate a cohesive powder. Adding polymer binder to the powder does not alter the resulting pore structure as long as the binder is completely dispersed.

Disks were formed from the milled powder by uniaxial compaction to increase density and provide cohesive strength for further handling. These disks were next pre-fired (23) at a temperature sufficient to remove the polymer binder and other volatile impurities, but at a rate low enough to minimize the formation of vapor pockets in the disks.

Finally, disks were sintered at very high temperatures and long exposure times to facilitate binding between individual Al_2O_3 grains through flow of material and migration of grain boundaries (3,24). While this process is performed to increase disk strength, some densification also occurs as grains grow or shrink in order to reduce the total grain surface area and thus minimize overall system free energy. Since this process eliminates void space, a small amount of magnesium oxide (MgO) was added to the powder mixture to inhibit alumina grain growth (24,25). Use of larger monodisperse and narrowly polydisperse alumina powders also facilitated reduction of grain growth and densification over the sintering times studied in this work.

Percolation Theory

The pore structure resulting from the fabrication method described above is very complex and difficult to model in detail; nonetheless, certain characteristics of this structure must be understood to properly design devices for transport control. A useful approximation that relies on observation of certain macroscopic properties to predict the pore volume and structure may be obtained through percolation theory.

Percolation theory is a statistical method of describing the behavior of random systems or processes. Power law relationships describing the behavior of these processes (e.g., diffusion of a molecule through a porous body) may be developed using the random walk model. Aspects of the overall field of percolation theory (2,26) considered pertinent to this work are described next.

The lattice concept is a convenient means of approximating the node–link–blob model of the porous alumina disk microstructure. A sample two-dimensional square lattice is shown in Fig. 1. In this structure, the corners of the squares represent nodes, the sides of the squares represent links, and the centers of the squares represent blobs. In this example, each blob is adjacent to up to four other blobs, thus giving a coordination number (z) of four. The magnitude of z reflects the complexity of the lattice.

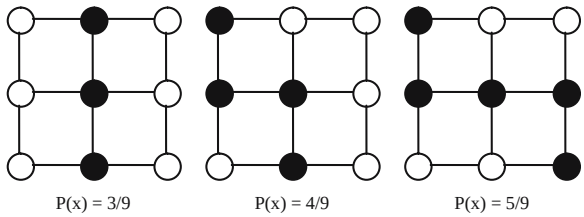

Fig. 1. Probabilities of occupied sites (*black circles*) crossing a finite two-dimensional square lattice.

This work utilized a site percolation model to describe the random walk between sites. This model assumes that each blob, or site, x exists with a probability P(x). Movement can only occur between adjacent existing sites. The alternative, known as a bond percolation model, assumes that all sites are present but that each bond x exists with probability P(x). In this case, movement can only occur between adjacent sites across existing bonds. Percolation in a real system may follow either model or be a combination of the two (27).

Two assumptions required by percolation theory are that the arrangement of sites is statistically random, and that the lattice is infinite in length. The assumption of infinite length allows values of P(x) that might vary widely in a finite system to converge to a single value. For example, the probability that sufficient occupied sites exist to span the square shown in Fig. 1 (a finite lattice) could be either 3/9, 4/9, or 5/9. These values would converge in an infinite lattice to a well-defined and unique value.

A cluster refers to a group of contiguous sites in the lattice, while the composite of all occurrences of a given cluster type in the lattice may be referred to as some type of lattice porosity. Key properties of a cluster are described relative to whether it spans the lattice, exists entirely within the lattice, or possesses at least one site on the lattice surface but terminates within the lattice or loops back to the same surface. The latter two cluster types are generally known as isolated clusters, while the first type is called an accessible cluster. The point at which an isolated cluster achieves sufficient length to span the lattice (known as a sample spanning cluster) is called the critical percolation threshold $\varnothing_c$. The composite of all isolated clusters is the isolated volume fraction ($\varnothing^I$), while the composite of all accessible clusters is the accessible volume fraction ($\varnothing^A$).

The coordination number z of a three dimensional infinite lattice may be estimated from its critical percolation threshold using the approximation shown in Eq. (1) (28).

$$\varnothing_c \approx 1/(1 + 0.356\, z) \tag{1}$$

Obviously, the value of $\varnothing_c$ decreases as the lattice becomes more complex. In the case of a cubic lattice, for which $z = 6$, Eq. (1) predicts a critical percolation threshold of 0.319.

All clusters are considered to be isolated for $\varnothing < \varnothing_c$. By definition, $\varnothing^A \equiv 0$ when $\varnothing < \varnothing_c$. Various elements of the total lattice porosity are defined by Eqs. (2a) and (2b) (29).

$$\varnothing = \varnothing^A + \varnothing^I; \tag{2a}$$

$$\varnothing^A = \varnothing^B + \varnothing^D, \varnothing \geq \varnothing c. \tag{2b}$$

In Eq. (2b), $\varnothing^B$ refers to the backbone volume fraction and $\varnothing^D$ refers to the dead-end volume fraction. The backbone represents that part of the multiply-connected sample-spanning cluster through which transport takes place. Dead-end clusters are branches of the backbone that do not contribute to transport at steady-state. Isolated clusters continue to exist above $\varnothing_c$, but their relative volume decreases rapidly as $\varnothing$ increases. The various volume fractions are represented for a two-dimensional square lattice in Fig. 2.

The above volume fractions taken in total represent a macroscopic means of describing the actual microstructure. These porosities do not require intimate knowledge of pore dimensions and distribution as long as the requisite percolation theory assumptions are satisfied. However, the dimensioning and volume displacement techniques (e.g., helium pycnometry) used to measure these quantities may not be sufficient to capture the influence of the microstructure on transport, as helium can enter pores that would be too small and/or convoluted to be accessible to water or contribute to transport. For this reason, a transport-dependent quantity, the effective diffusivity ($\varnothing^E$), is defined as the diffusivity (normalized to the aqueous diffusivity) resulting from the transport resistance of the lattice. Although $\varnothing^E$ may be thought of as a subset of $\varnothing^B$ (i.e., $\varnothing^E \leq \varnothing^B$), it is not rigorous to compare the two quantities directly as the former depends on properties of the transport system (solvent, solute, etc.) while the latter reflects the pore structure available for transport. The critical percolation threshold should, however, be the same for both the structural and transport-dependent models as long as the infinite lattice assumption is valid.

Scaling laws may be used to represent relationships between total lattice porosity and structural or transport-dependent quantities above $\varnothing_c$. Such laws are based on the power law expansion as shown in Eq. (3).

$$\boldsymbol{f}(y) \propto (y - y_0)^{\alpha} \tag{3}$$

Eq. (3) relates the value of a property $\boldsymbol{f}(y)$ to the magnitude of the deviation $y - y_0$. Here y represents some independent property and y_0 represents some initial or critical state of that property. Different properties are affected differently by $y - y_0$ through the value of some critical exponent α, which is referred to as a universal exponent because it typically

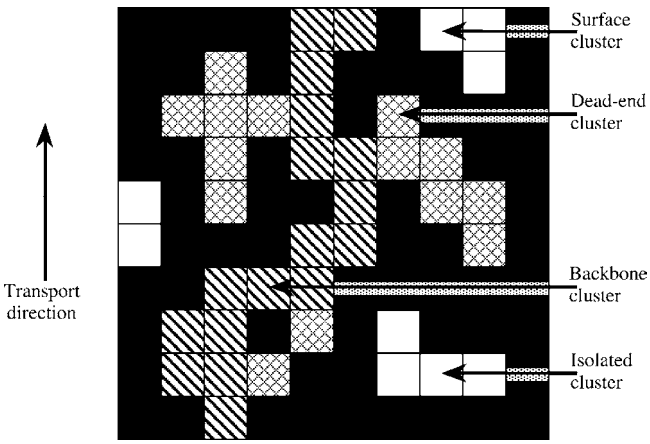

Fig. 2. Types of pore clusters on a two-dimensional square lattice.

depends only on the dimensionality of the system and not on y or y_0. It is this system dimensionality that is influenced by the site probability P(x) through the average coordination number. The value of α will also be influenced by whether the scaling law in question is based on a site or bond approach; in this work, all critical exponents are based on a site percolation model.

Examples of scaling laws exist in the literature for both the structural and transport cases. In the structural case, the accessible volume fraction above the percolation threshold may be modeled by Eq. (4),

$$\varnothing^{A} \propto (\varnothing - \varnothing_c)^{\beta}, \tag{4}$$

which is valid for $\varnothing > \varnothing_c$. β is the universal scaling exponent in this relationship, and has been reported (28) as equal to 0.4 in three dimensions. The backbone volume fraction, being a subset of the accessible volume fraction, may likewise be defined (28) as shown in Eq. (5).

$$\varnothing^{B} \propto (\varnothing - \varnothing_c)_B^{\gamma} \tag{5}$$

γ_B is the backbone lattice exponent with value 0.9 in three dimensions.

In the transport-dependent case, aqueous diffusion is enabled by the backbone volume fraction. This diffusion may be modeled as shown in Eq. (6) (30).

$$\varnothing^{E} \propto (\varnothing - \varnothing_c)^{\mu} \tag{6}$$

In this case, μ is known as the conductivity exponent with value 2.0 in three dimensions. The value of μ has been estimated in the literature through conductivity measurements near the percolation thresholds of conductor/insulator mixtures (31–33), hence the name given to this parameter.

Values of $\varnothing^{I}$ and $\varnothing$ may be obtained directly through dimensional and volume displacement measurements. The effective diffusivity $\varnothing^{E}$, however, must be derived by measuring resistance to transport through the lattice and comparing this resistance to the bulk (i.e., no resistance) transport case. In the case of aqueous diffusion of a small molecule, $\varnothing^{E}$ may be obtained by measuring the steady state transport rate through a lattice placed between an infinite source and an infinite sink, estimating the diffusivity corresponding to this rate, and comparing this diffusivity to the bulk aqueous diffusivity. $\varnothing^{E}$ is then defined by Eq. (7) (28),

$$\varnothing^{E} = D_B/D_{aq}, \tag{7}$$

where D_B is the diffusivity due to the resistance of the lattice and D_{aq} is the bulk aqueous diffusivity. Eq. (7) is valid as long as the mean free path of the random walk of the molecule is smaller than the pore diameter, in which case Knudsen diffusion is not expected to occur.

Eq. (6) is only strictly valid near $\varnothing_c$. As $\varnothing$ increases, transport approaches the conventional relationship of path length (L) to time (t) shown in Eq. (8).

$$L^2 = D_B t \tag{8}$$

This equation diverges as $\varnothing \rightarrow \varnothing_c$.

Trends in the various volume fractions as functions of total porosity are shown in Fig. 3 for a three dimensional cubic lattice. These trends hold for an infinite system, but diverge as the pore size approaches the system length. This results in the various quantities shown in Fig. 3 converging to finite minima rather than zero as $\varnothing \rightarrow \varnothing_c$. Finite-size scaling may be used to modify the above scaling laws to accommodate finite system length.

It was a goal of this work to model the behavior of $\varnothing^{E}$ near $\varnothing_c$ for a finite system length to demonstrate how drug release might still be achieved in ceramic devices of reduced porosity (for higher strength). A modification to Eq. (6) for this case has been suggested in the literature as shown in Eq. (9) (5,7),

$$\varnothing^{E} \propto L^{-\mu/\nu} \Phi\left[(\varnothing - \varnothing_c) L^{1/\nu}\right], \tag{9}$$

where L is the system length, ν is a correlation length exponent with value 0.9 in three dimensions (2), and Φ is a finite, positive function valid for $\varnothing$ within about ±10% of $\varnothing_c$. The accepted criterion (34) for onset of finite-size effects is $d/L > 1/50$, where d is the mean pore diameter. For purposes of this study, L is defined as being equal to the system length divided by the number of voids required to cross that length.

In keeping with other work performed in our laboratory (17,18,35), the extremely complicated pore morphology of a sintered alumina device makes it an ideal candidate for study using percolation theory. Other work has shown that the average ceramic microstructure may be approximated using a 14-sided polyhedron known as a tetrakaidecahedron (5). This

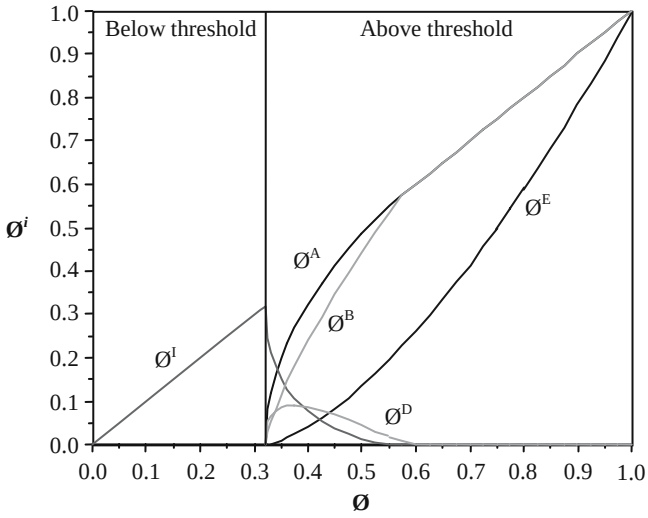

Fig. 3. Individual volume fraction trends as functions of total porosity ($\varnothing$) for a three-dimensional cubic lattice (2). $\varnothing^{i}$ represents the pertinent volume fraction, with i = A, B, D, E, or I.

polyhedron has a coordination number $z = 14$ and a site percolation threshold (obtained by Monte Carlo transport simulations) $\varnothing_c = 0.17$. Whether or not alumina devices made in this laboratory possessed structural and transport characteristics similar to those of the tetrakaidecahedral lattice was addressed through comparison of experimental and simulated values of $\varnothing_c$. D_B was obtained for this purpose by applying a membrane transport model to diffusion through the alumina matrix.

Little previous experimental work addresses the actual disappearance of the structural percolation parameter $\varnothing^A$ as $\varnothing \rightarrow \varnothing_c$ as predicted by simulation. As it was observed through experiment that $\varnothing^A$ could not be estimated directly using Eq. (4), it was important to show whether acceptable values of $\varnothing^A$ could be obtained through direct measurement of $\varnothing^I$ and $\varnothing$ both above and below the percolation threshold.

Finally, it was of interest to demonstrate finite-size scaling behavior by artificially enlarging the pores in the matrix, thereby forcing $d/L > 1/50$. In such a system, anomalously high values of D_B should be observed at the value of $\varnothing_c$ obtained for an infinite lattice, and the function Φ should be obtainable from this high diffusivity.

Drug Delivery Applications of Alumina

Oxide ceramics, of which alumina is an example, are commonly used as structural materials in the human body due to their bioinertness, resistance to corrosion, and high tensile strength (36,37). These properties make oxide ceramics attractive for such uses as bone and tooth replacements. Presence of significant porosity in the body of such a structural ceramic is a disadvantage in these applications, since this porosity will decrease the strength of the body.

The *in vivo* behavior of porous oxide ceramics has not been widely studied; nonetheless, the same properties that make alumina attractive as a structural biomaterial (bioinertness and strength) could be used to advantage as a porous implantable carrier for delivery of drug molecules (38). For example, a porous ceramic body could be used as a reservoir release device, wherein the ceramic acts as the walls of the device and a solid drug is loaded into the hollow center. The device would then be sealed shut and implanted. Fluid would enter the reservoir through the pores of the ceramic and solubilize the drug, which would then diffuse out of the device as a saturated solution. Release of the drug, which would depend on both the porosity of the matrix and the saturation concentration of the drug, could then be modeled using percolation theory. The release rate of the drug could be manipulated by varying the pore structure of the ceramic walls. Alumina reservoir devices would be most suitably placed in or near areas of hard tissue, so as to ensure that no damage to soft tissue could occur due to the presence of a hard foreign body.

Alternatively, a drug could be dispersed in the pores of a ceramic matrix by first permeating the matrix with a solution of drug and then drying in some manner (e.g., lyophilization). The pore structure of the matrix and the solubility of the drug would dictate the release behavior of the device. Finally, ceramic matrices could be used to immobilize enzymes and/or act as filters for convective transport processes such as dialysis. The required drug loading in and/or release behavior of such a device could be described and predicted using the concepts of percolation theory described here.

MATERIALS AND METHODS

Materials

Sintered ceramic disks were composed of 99.5% w/w Al_2O_3 (99.8%, lot #00521PM, Aldrich Chemical Co., Milwaukee, WI) and 0.5% w/w MgO (99.5%, lot #H11G, Morton Thiokol Inc., Alfa Products, Danvers, MA). PVP (lot #G707, GAF Corp., Wayne, NJ) of average molecular weight 10,000 Da was used as a binder. Composition of a typical 100 g dry powder batch containing (for example) 10% w/w binder was 10 g PVP, 0.45 g MgO, and 89.55 g Al_2O_3.

Aldrich Al_2O_3 powder was polydisperse with a nominal diameter range of 1–10 μm as reported by the vendor. Median diameter of this powder was not obtained. To judge the processing properties of this powder against those of a more monodisperse powder, disks were also made using 0.5 μm diameter monodisperse Al_2O_3 (99.7%, Realox alumina powder, lot #XA-1000, Alcoa Chemicals Inc., Pittsburgh, PA).

Alumina Processing

Al_2O_3, MgO, and PVP powders were dry-mixed on a piece of parchment paper using a large steel spatula. PVP binder contents ranged from 5 to 20% w/w. Dry-mixed powders were next charged to a Pyrex petri dish and formed into a wet slurry by addition of enough distilled deionized water (Sybron-Barnstead, Boston, MA) to completely wet the mixture. This slurry was stirred for 5 min using a rubber policeman, covered, allowed to settle for 24 h, stirred again, and then dried in a Precision Scientific Co. model 10 vacuum oven at 12.28 psig vacuum and 110°C. The dried powder cake was pulverized in a porcelain mortar and pestle and stored in an airtight glass jar.

Unfired disks were manufactured by compressing the dried powder mixture into a disk shape using a Carver model C laboratory press in which pressure was applied uniaxially to the top of the sample. Compaction pressures ranged from 1,000 to 10,000 psig. A custom type 308 stainless steel tablet punch was used to compress each powder mixture. Each disk was made to a target weight of between 0.6 and 0.7 g.

Pressed disks were pre-fired at 1,100°C to remove water, binder, and volatile impurities using a Lindberg model 51848 Moldatherm box furnace. Heating temperature was ramped at a controlled rate to ensure thermal equilibrium in the compacts. Pre-fired disks were next sintered at high temperature using a Lindberg model 51314 1,700°C box furnace with six molybdenum disilicide heating elements. Sintering followed a heating schedule in which temperature was increased at 30-min intervals to ensure thermal equilibrium. Maximum sintering temperatures ranged from 1,450 to 1,670°C, for times lengths of 1 to 36 h. Sintered disks were cooled at 1,300°C for 1 h before being allowed to cool to room temperature for 4 to 5 h. The target sintering temperature was achieved as quickly as possible in order to minimize contribution of lower temperatures to the overall densifica-

tion process. Cooling occurred in two stages to minimize the potential for disk cracking due to thermal stress.

A Thermolyne Type 46100 1,700°C box furnace (Department of Water Chemistry, University of Wisconsin) was used in one study to gauge the effects of ramping rate (5 to 30°C/min), maximum sintering temperature (1,450 to 1,670°C), and sintering time (1 to 12 h) on the final porosities of sintered disks made using both Aldrich polydisperse and Alcoa monodisperse Al_2O_3 powders.

Sintered disks were washed by bathing and sonicating in denatured HPLC grade ethyl alcohol (lot #05103BW, Aldrich). Washed disks were then dried in the Moldatherm furnace at 750°C.

Total Porosity Determination

Total porosities of sintered disks were determined by two methods. Dimensional measurements of disks were obtained with a Vernier caliper and micrometer and used to calculate $\varnothing$ per Eqs. (10a) and (10b),

$$\rho_{bulk} = M_{disk}/[1\ \pi\ d^2/4], \tag{10a}$$

$$\varnothing = 1 - \rho_{bulk}/\rho_{theor}, \tag{10b}$$

where M_{disk} is the dry disk mass, ρ_{bulk} is the measured disk density, ρ_{theor} is the density of the alumina crystal (4.0 g/cm^3), l is the mean disk thickness, and d is the mean disk diameter (n = 5 for each mean).

Dimensional measurements were prone to error as disks did not shrink evenly during sintering; thus, an Archimedes volume displacement method (1,3) was also used to measure buoyant weight of a disk. In this case, ρ_{bulk} is calculated using Eq. (11),

$$\rho_{bulk} = \rho_1 M_{disk}/[M_3 - M_2], \tag{11}$$

where M_3 is the weight of disk plus any imbibed solution, M_2 is the buoyant disk weight, and ρ_1 is the density of suspending liquid. Mean disk densities (n = 5) were determined in this manner using a Mettler model 33340 density kit with a solution of approximately 86% glycerol/water (99.5+% spectrophotometric grade glycerol, lot 05902, Aldrich). Disks were dried at 750°C to remove imbibed solution. Disk volumes obtained by the Archimedes method were observed to be more precise than those obtained by dimensional measurement, and were thus used to calculate percolation properties in the remainder of the work.

Structural Volume Fraction Determination

True disk volumes (i.e., solid grains plus isolated pore space) were obtained using a Quantachrome Multipycnometer model MVP-1 with helium as the displacement gas. Helium was assumed to penetrate all but the isolated volume fraction of a given disk.

True volumes (V_s) of batches of five disks each were calculated using Eq. (12) (1),

$$V_s = V_{cell} - V_{ref}[[P_1/P_2] - 1], \tag{12}$$

where V_{cell} and V_{ref} are calibrated sample cell and reference cell volumes, and p_1 and p_2 are original and final system pressures. Isolated volume fractions were then calculated from mean V_s results (n = 10 per batch) using Eq. (13),

$$\varnothing^I = [V_s/V_t] - [1 - \varnothing], \tag{13}$$

where V_t and $\varnothing$ are the total bulk volume and mean total porosity of the disk batch.

Note that $\varnothing^I$ as it appears in Eq. (2a) refers to all non-sample spanning clusters, regardless of whether such clusters are truly inaccessible or are exposed to one surface of the system. Both types of cluster are shown in Fig. 2. Helium pycnometry only provides information regarding the truly inaccessible cluster volume. Thus, since the assumption that $\varnothing - \varnothing^I = 0$ for $\varnothing < \varnothing_c$ (since $\varnothing^A \equiv 0$) will not be true when $\varnothing^I$ is determined using helium pycnometry, the difference between $\varnothing$ and $\varnothing^I$ for $\varnothing < \varnothing_c$ was referred to in this work as the surface volume fraction ($\varnothing^S$) so as to not confuse the nonzero accessible volume fraction existing for $\varnothing < \varnothing_c$ with the accessible volume fraction as defined in Eq. (4). Using these definitions, Eq. (2a) may then be rewritten as Eqs. (14a) and (14b).

$$\varnothing = \varnothing^I + \varnothing^S, (\varnothing < \varnothing_c); \tag{14a}$$

$$\varnothing = \varnothing^I + \varnothing^A, (\varnothing \geq \varnothing_c). \tag{14b}$$

Since, when using helium pycnometry, it is never the case that $\varnothing - \varnothing^I = 0$ for all $0 < \varnothing \leq 1$, results obtained by this technique give the appearance of being influenced by finite-size scaling. Nonetheless, the discontinuity in $\varnothing^I$ that occurs at $\varnothing = \varnothing_c$ may still be used to estimate $\varnothing_c$ from the values of $\varnothing^A$ calculated using Eq. (14b) as will be discussed below.

Mercury porosimetry and scanning electron microscopy were also performed in the broader work (1) to gain a qualitative idea of disk microstructure; however, as these techniques were not required to estimate $\varnothing_c$ nor to demonstrate finite size scaling, they will not be discussed in this paper.

Effective Diffusivity Determination

Effective diffusivities for transport were estimated using a Stokes diaphragm cell as shown in Fig. 4. Donor and

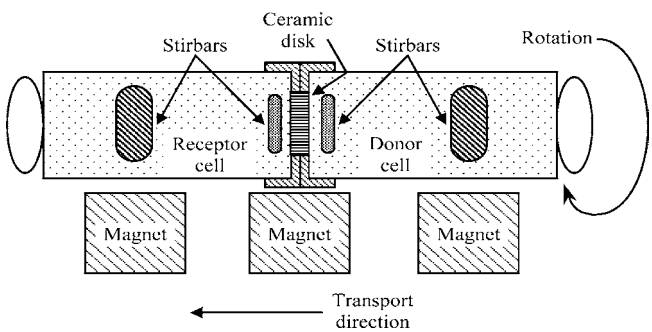

Fig. 4. Representation of a Stokes diaphragm cell (4). Cell is actually mounted in the vertical position, but is shown here in a horizontal orientation for convenience. Figure not to scale.

receiver compartments were constructed of Kimax borosilicate glass. Disks were cemented in Lucite using Torr–Seal epoxy and then mounted between the two glass compartments. Cells were clamped vertically in Talboys t-line laboratory stirrers and rotated at 100 rpm. Magnetic Teflon stir bars used to agitate the compartment contents were immobilized relative to cell motion using alnico horseshoe magnets. The two small stirbars were positioned as close to the disk faces as possible to minimize boundary layer resistance to transport, while the two larger stirbars were used to agitate the bulk solutions.

Both donor and receiver compartments contained a pH 6.9 phosphate buffer solution of 0.025 M K_2HPO_4 (Aldrich, anhydrous, ACS reagent, lot 03420AW), and 0.025 M KH_2PO_4 (Aldrich, 99%, ACS reagent, lot #03322KV), along with 50 μg/ml 4-fluorobenzoic acid (FBA; Aldrich, 99%, lot 02818BV) as an internal liquid chromatography standard and 250 μg/ml propyl 4-hydroxybenzoate (PB; Aldrich, 99+%, lot 00712TM) as a preservative (39). In addition to the above, the donor compartment contained 250 μg/ml benzoic acid (BA; Aldrich, 99+%, ACS reagent, lot 10020 LV) at t = 0. BA ($pK_a = 4.03$) was assumed to be 99.9% ionized at pH 6.9. Hindrance of benzoate ion diffusion due to electrical interaction with the ceramic matrix was not expected to occur at steady-state. Disks were perfused with the above solution prior to initiation of each transport experiment.

To determine diffusivity of BA across a ceramic disk, solution samples of 0.5 μl were removed from the receiver cell every 3 to 5 days and analyzed for BA content using high performance liquid chromatography. Concentrations were measured using a Waters model 440 ultraviolet absorbance detector using a 254 nm wavelength lamp and set at 0.05 absorbance units full scale. Separation columns included a Beckman Ultrasphere ODS (5 μm, 4.6 mm × 25 cm, serial #9UE787) reversed-phase C18 column and a Beckman Ultrasphere ODS (5 μm, 4.6 mm × 4.5 cm, serial #7D14) matched precolumn. The mobile phase was composed of 54% v/v H_2O, 35% v/v methanol (Baxter, spectrophotometric grade, lot AW042), 10% v/v acetonitrile (Aldrich, HPLC grade, lot 10201TW), and 1% v/v acetic acid (Aldrich, 99.7+%, ACS reagent, lot 03210JT) to neutralize benzoate ion.

Achievement of steady-state BA transport across a disk was defined as the point beyond which a profile of receiver cell BA concentration *vs.* time became linear. Five time points beyond this were usually sufficient for calculation of D_B using Eq. (15) (1),

$$D_B = {}^1/_{\beta t} \ln \left[(c_{don} - c_{rec})^0 / (c_{don} - c_{rec})^t \right], \qquad (15)$$

where β is a constant that depends on the Stokes cell configuration, t is elapsed time at steady state, c_{don} and c_{rec} are the donor and receiver cell BA concentrations, and t = 0 refers to initiation of steady-state. Eq. (15) was obtained using a pseudosteady-state approximation to first order membrane transport (4).

The aqueous diffusivity of benzoate ion in pH 6.9 phosphate buffer at 25°C was obtained by injecting a 250 μg/ml benzoate ion solution into a Taylor dispersion apparatus placed in series with a Beckman model 160 variable wavelength absorbance detector at 254 nm (1,4). A value of $D_{aq} = 1.45 \times 10^{-5}$ cm^2/s, representing a mean of 11 trials, was obtained using the Taylor dispersion apparatus. This value is analogous to that reported by Higuchi *et al.* (40) for BA diffusivity in 0.01 N HCl (1.4×10^{-5} cm^2/s) using a diaphragm diffusion cell.

Finite Size Scaling of Effective Diffusivity

In the finite-size scaling experiment, polymer microspheres of known diameter were blended into batches of Aldrich alumina/MgO/5% PVP that had been made by wet mixing. Microspheres were obtained from Duke Scientific Co. and consisted of either poly(styrene) divinylbenzene (PVS/DVB; ρ = 1.05 g/cm^3) or poly(methylmethacrylate) (PMMA; ρ = 1.19 g/cm^3). Microsphere properties are summarized in Table I.

Four powder batches, each with enough spheres to account for 10% of the estimated final total volume of a typical disk, were made as listed in Table II. Pre-fired disks were sintered using the Lindberg furnace in the Department of Water Chemistry at a heating rate of 10°C/min and a maximum sintering temperature of 1,670°C. Ten disks were pressed from each batch, with five disks then being sintered for 12 h and five for 24 h. Firing times were chosen to eliminate as much residual porosity as possible based on the results of previous experiments.

RESULTS

Porosity Control

Details of investigations into control of sintered alumina disk porosity are summarized elsewhere (1). In summary, the four parameters being observed to have the greatest impact on disk porosity were alumina powder polydispersity, compaction pressure, sintering temperature, and time at temperature. Disks made using polydisperse alumina powder were found to have much higher total porosities than disks made using monodisperse alumina powder regardless of other

Table I. Properties of Poly(Styrene) Divinylbenzene (PVS/DVB) and Poly(Methylmethacrylate) (PMMA) Microspheres Used in Finite-Size Scaling Study

Sphere Type	Mean Diameter (μm)	Lot Number	Spheres per Gram (×10^3)	Total Weight (g)	Volume per Sphere (cm^3×10^{-6})
PVS/DVB	136 ± 2.7	9276	720	1	1.39
PVS/DVB	282 ± 5.6	10010	81	2	12.3
PVS/DVB	468 ± 9.4	9513	18	2	55.6
PMMA	773 ± 15	8543	4	2	250

Table II. Compositions of Powder Batches Used in Finite-Size Scaling Study

Powder Batch	Sphere Content (% v/v)	Alumina (g)	MgO (g)	PVP (g)	Spheres Used (g)
1	10	12.00	0.06	0.64	0.3165
2	10	11.99	0.06	0.64	0.3158
3	10	11.99	0.07	0.64	0.3117
4	10	12.00	0.06	0.65	0.3108

process conditions. Examples of relative disk porosities obtained using polydisperse and monodisperse powders are shown in the context of other process studies below.

As expected, pressures used to compress unfired disks from polydisperse Al_2O_3 powder impacted final sintered porosity as shown in Fig. 5a. Based on this result, compaction pressures of 10,000 psig were chosen for further work in order to produce void volumes closer to the proposed percolation threshold of 0.17 and to avoid the impact of small variations in compaction pressure on void volume that would be anticipated at low pressures.

Dependencies of sintering temperature and time at temperature for disks made using both polydisperse and monodisperse alumina powders are shown in Fig. 5b and c. These results indicate that some control of porosity in polydisperse disks is possible using these parameters. The sintering process in monodisperse disks was seen to be essentially complete after only one hour of heating at all evaluated temperatures. It was observed that monodisperse disks could not be made with $\varnothing$ above the expected value of $\varnothing_c$.

For a set particle size or range of polydispersity, the final porosity and extent of densification was influenced most strongly by the sintering temperature. In this work, however, sintering time was used to vary disk porosities since time could be manipulated more conveniently than temperature given the equipment at hand and also because the target porosity range could be obtained through firing time alone. Monodisperse powders were used to generate disks with low total porosities (i.e., $\varnothing < \varnothing_c$), while polydisperse powders were useful at achieving higher porosities. Other aspects of the investigation indicated that the microstructures of disks made using both types of alumina powder were sufficiently similar to enable grouping of data from these disks into a single percolation theory model, as per Fig. 3, to expand the

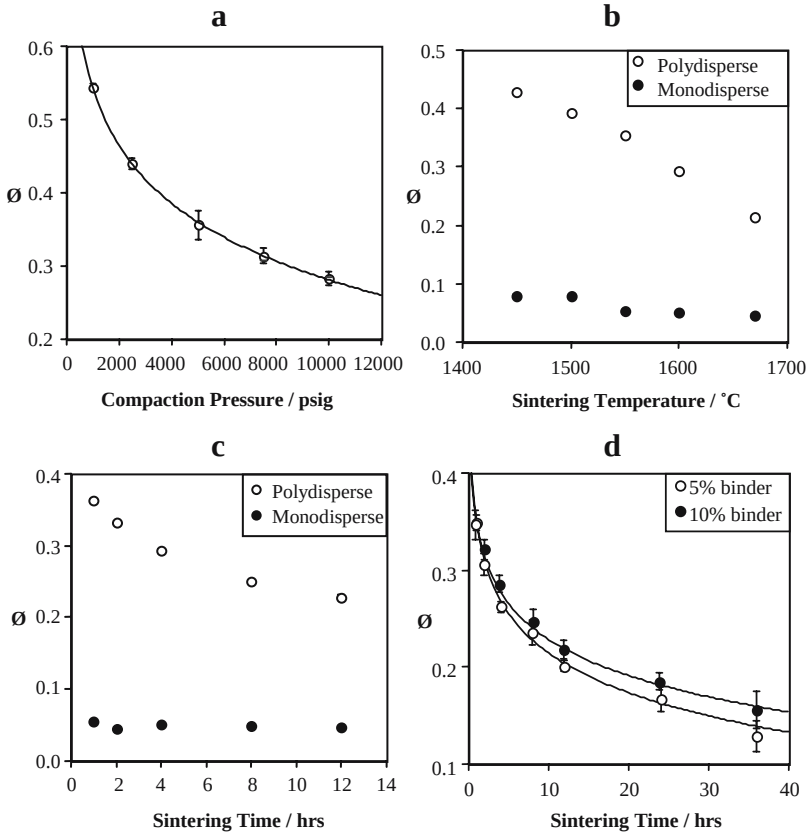

Fig. 5. (a) Influence of applied compaction pressure on total porosity ($\varnothing$) for polydisperse alumina disks. 10% PVP, sintering time 4 h, sintering temperature 1670°C. (b) Dependence of $\varnothing$ on sintering temperature and powder polydispersity. 5% PVP, compaction pressure 10,000 psi, sintering time 4 h. (c) Dependence of $\varnothing$ on sintering time and powder polydispersity. 5% PVP, compaction pressure 10,000 psi, sintering temperature 1600°C. (d) Dependence of $\varnothing$ on binder content and sintering time for polydisperse alumina disks. Compaction pressure 10,000 psig, sintering temperature 1670°C.

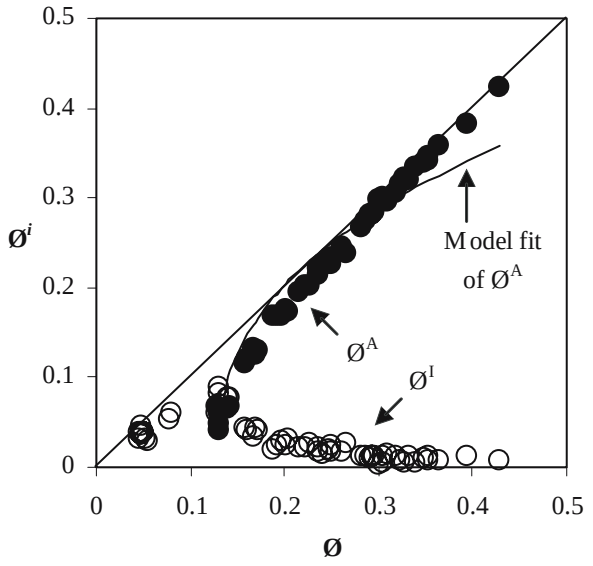

Fig. 6. Isolated ($\varnothing^{I}$) and accessible ($\varnothing^{A}$) volume fraction results for $\varnothing \geq \varnothing_c$. *Line* represents fit of Eq. (18) using experimental values of total porosity ($\varnothing$). $\varnothing^{i}$ represents the pertinent volume fraction, with i = A or I.

achievable range of $\varnothing$. Similar groupings were performed for disks made at different sintering temperatures.

Finally, binder content had some impact on total porosity (mostly at longer sintering times) as shown in Fig. 5d. The slight reduction in total porosity achieved at 5% w/w binder content was useful in generation of disks with porosities closer to the expected value of $\varnothing_c$ than were possible using 10% w/w binder.

Determination of $\varnothing^{A}$

Disks of varying porosities were made using both monodisperse and polydisperse alumina powders, 5 and 10% w/w PVP binder contents, 10,000 psig compaction pressure, 1,670°C sintering temperature, and a range of sintering times. Reproducible total porosities were obtained using the Archimedes volume displacement method. Total porosities ranged from 0.045 to 0.080 for monodisperse alumina disks and 0.129 to 0.429 for polydisperse alumina disks.

Isolated volume fractions were determined by helium pycnometry. Below $\varnothing_c$, $\varnothing^{A} \equiv 0$ and $\varnothing$ is calculated using Eq. (14a). At and above $\varnothing_c$, $\varnothing^{A}$ is calculated using Eq. (14b). Because helium pycnometry only measures the true isolated volume fraction $\varnothing^{I}$, no distinction can be made between sample-spanning and non-sample spanning accessible clusters above $\varnothing_c$.

As was illustrated in Fig. 3, $\varnothing^{I}$ should increase linearly as $\varnothing \rightarrow \varnothing_c$ from below but then decay rapidly above $\varnothing_c$. This behavior should hold regardless of whether $\varnothing^{I}$ is composed of all non-sample spanning clusters (per Eq. 2a) or only reflects the inaccessible cluster volume (per Eq. 14a). Those disks for which $\varnothing^{I}$ is increasing with increasing $\varnothing$ may then be assumed to have total porosities $\varnothing < \varnothing_c$. $\varnothing^{S}$ was calculated for these disks by subtracting $\varnothing^{I}$ from $\varnothing$. The monodisperse alumina disks made in this work were found to exhibit values of $\varnothing^{I}$ in this range.

On the other hand, values of $\varnothing^{I}$ obtained experimentally for polydisperse alumina disks were observed to decrease rapidly with increasing $\varnothing$, implying that all polydisperse disks possessed porosities greater than $\varnothing_c$. $\varnothing^{A}$ was calculated for these disks by subtracting $\varnothing^{I}$ from $\varnothing$ per Eq. (14b). A nonlinear least squares fit of these $\varnothing^{A}$ results *vs* $\varnothing$ was then used to estimate $\varnothing_c$ for the structural case as shown in Eq. (16),

$$\varnothing^{A} = a(\varnothing - \varnothing_c)^{\beta}, \tag{16}$$

where a is a pre-exponential factor and $\beta = 0.4$. Results of this fit were $\varnothing_c = 0.128 \pm 0.001$ and $a = 0.58 \pm 0.01$. This value of $\varnothing_c$ was lower than the model prediction of $\varnothing_c = 0.17$ for a tetrakaidecahedral lattice. A fit of Eq. (16) using the expected value of $\varnothing_c = 0.17$ resulted in $\beta = 0.43 \pm 0.02$, which confirmed the applicability of the model but suggested that use of helium pycnometry may have resulted in underestimation of $\varnothing_c$.

Results of $\varnothing^{A}$ and $\varnothing^{I}$ *vs* $\varnothing$ for polydisperse alumina disks are summarized in Fig. 6. As may be seen from this figure, the model accurately predicted the value of $\varnothing_c$; however, the overall fit of the $\varnothing^{A}$ data was poor. Of course, the quality of the fit would be expected to deteriorate above a total porosity of about 0.25 to 0.3, because the scaling law becomes invalid as the influence of individual pores (especially of isolated pores) on the overall structure becomes less important and $\varnothing^{A} \rightarrow \varnothing$.

DETERMINATION OF $\varnothing^{E}$

Estimation of the effective diffusivity of a small molecule, $\varnothing^{E}$, was performed for 21 polydisperse alumina disks made using binder contents of 5% w/w and 10% w/w and sintering times of 1 to 24 h. Total porosities varied from 0.147 to 0.369, while effective volume fractions obtained using these disks ranged from 0.000 ($\varnothing = 0.147$) to 0.079 ($\varnothing = 0.368$).

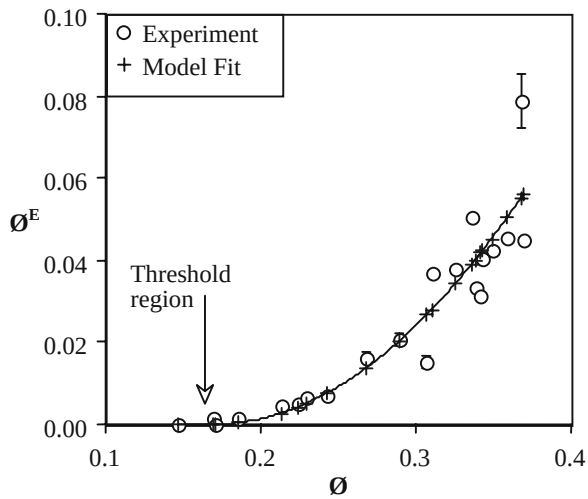

Fig. 7. Effective diffusivity ($\varnothing^{E}$) results. *Line* represents fit of Eq. (17) using experimental values of total porosity ($\varnothing$).

Table III. Disk Property Data for Finite-Size Scaling Study

Powder Batch	∅	Sintered Void Diameter (μm)	System Length (L)/Voids per Disk	$\varnothing^E$	$(\varnothing - \varnothing_c)L^{1/\nu}$	$\varnothing^E L^{\mu/\nu}$
1	0.178	121	14.170	0.018 (0.003)	0.171	6.514
2	0.185	250	7.359	0.024 (0.000)	0.147	2.025
3	0.188	415	4.195	0.028 (0.001)	0.093	0.678
4	0.190	685	2.468	0.034 (0.003)	0.057	0.253

Disks processed at compaction pressure 10,000 psig, sintering temperature 1,670°C, sintering time 12 h. Values in parentheses represent standard error of $\varnothing^E$ linear regression fit. Sintered void diameters assume 31% shrinkage due to processing.

A nonlinear least squares fit of all $\varnothing^E$ *vs* ∅ was used to estimate $\varnothing_c$ for the transport-dependent case as shown in Eq. (17),

$$\varnothing^E = b(\varnothing = \varnothing_c)^{\mu}, \tag{17}$$

where b is a pre-exponential factor and $\mu = 2.0$. Results of this fit were $\varnothing_c = 0.169 \pm 0.02$ and $b = 1.40 \pm 0.32$. This "transport-dependent" value of $\varnothing_c$ matched the prediction of $\varnothing_c = 0.17$ for a tetrakaidecahedral lattice (5).

A summary of all $\varnothing^E$ *vs* ∅ results is shown in Fig. 7. In this case, deviation of the model from experimental data appears to begin at $\varnothing \approx 0.35$ as implied by the increasing scatter in the $\varnothing^E$ *vs* ∅ results at higher values of ∅. This behavior is expected because the scaling law should, by definition, become invalid as ∅ increases and the contribution of individual pores to transport becomes less relevant.

Finite-Size Scaling

Finite-size scaling is possible in any system in which the pore cluster diameter is the same order of magnitude as the linear thickness of the disk. Such a system will exhibit transport that is anomalously high as compared to that expected on the infinite lattice. This effect can only be seen within ±10% of the percolation threshold, as it is swamped out at higher porosities. The transport-dependent percolation threshold obtained for the infinite lattice is also assumed to be valid for a finite-size system for the purposes of modeling, but $\varnothing^E$ will not necessarily be equal to zero at this threshold.

An increase in the experimental value of $\varnothing^E$ above the value that would be expected on the infinite lattice for a given total porosity is an indication of finite-size scaling. In this study, finite-size scaling was implemented by using polymer microspheres that left large pore bulbs in the disk structure after pre-firing. ∅ was held approximately constant by varying sphere concentration in accordance with sphere diameter, thus increasing individual pore bulb diameter without substantially increasing total porosity. A slight increase in total porosity observed with increasing sphere diameter was assumed not to be significant compared to the effect of changing bulb volume.

Values of $\varnothing^E$ were determined using disks made from the four powders listed in Table II. Disks were sintered at 1,670°C for 4 h. The number of bulb diameters (L) required to cross the linear thickness of each disk was calculated after sintering, with the assumption being made that the amount of volume shrinkage due to sintering was approximately 31%. Data obtained from Stokes diaphragm cell experiments were then used to calculate $\varnothing^E$ for each disk using Eq. (7). Results are summarized in Table III.

$\varnothing^E$ results for four disks (average total porosity 0.185) of increasing L are shown in Fig. 8. $\varnothing^E$ is seen to initially decrease rapidly with increasing L and then level off. As L

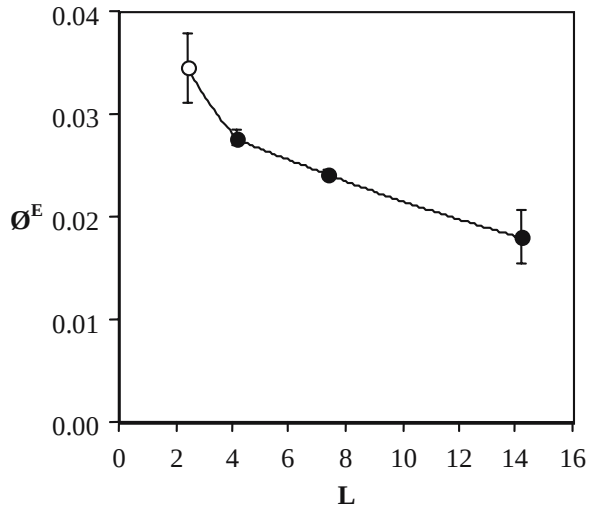

Fig. 8. Finite-size scaling study, dependence of $\varnothing^E$ on system length (L) for disks with ∅ = 0.185 and $\varnothing_c = 0.169$. L is expressed as the number of voids required to span the disk. *Open circle* represents voids made using PMMA microspheres; *filled circles* represent voids made using PVS/DVB microspheres.

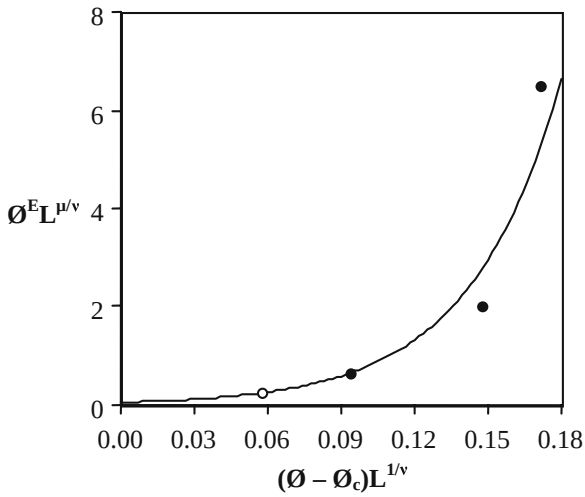

Fig. 9. Finite-size scaling study, plot of $\varnothing^E L^{\mu/\nu}$ *vs* $(\varnothing - \varnothing_c)L^{1/\nu}$. *Open circle* represents voids made using PMMA microspheres; *filled circles* represent voids made using PVS/DVB microspheres.

approaches infinity, $\varnothing^E$ should assume its limiting value for an infinite lattice of total porosity $\varnothing$.

The value of the function $\Phi(\varnothing,L)$ in Eq. (9) was estimated through a fit of $\varnothing^E L^{\mu/\nu}$ *vs* $(\varnothing - \varnothing_c)L^{1/\nu}$ as shown in Fig. 9. This fit is summarized as Eq. (18).

$$\varnothing^E \propto L^{-\mu/\nu} \exp\left[(\varnothing - \varnothing_c)L^{1/\nu}\right], \tag{18}$$

The value of the exponential term goes to one at the limit of $\varnothing \rightarrow \varnothing_c$, with the result that $\varnothing^E$ scales as $L^{-\mu/\nu}$ below $\varnothing_c$ rather than falling to zero as in the infinite case. This result has also been demonstrated by others (5,7). Equation (18) is not valid for an infinite lattice because the exponential term becomes infinite as $L \rightarrow \infty$.

DISCUSSION

Production of Porous Ceramics

Polydisperse alumina was determined to be an ideal powder for use in manufacturing disks of controlled porosity and low shrinkage. Sintering temperature and powder polydispersity were found to exert the greatest control over final disk porosity, although sintering time rather than temperature was used to control porosity in this work due to equipment limitations.

Total porosities of 15 to 40% were easily obtained and reproduced using polydisperse alumina powder, while very low porosities (4 to 10%) were only achieved with a monodisperse powder. Thus, it may be seen that some degree of polydispersity combined with moderate (i.e., between 1 and 10 μm) mean particle size is advantageous for retention of significant void space in the final disk. It is important to note that mean particle size and polydispersity are interrelated because very small polydisperse disks could exhibit considerable shrinkage while very large monodisperse disks could shrink very little.

The Percolation Theory Model

Percolation theory models were used to estimate both structural and transport-dependent values of $\varnothing_c$ (0.128 and 0.169, respectively), which were seen to differ significantly. Such disagreement may have resulted from incomplete filling of sample-spanning pores by the transport medium, or alternatively from some fundamental deficiency in the structural model. Because the structural backbone porosity is that fraction of the accessible porosity thought to be used in steady state transport, and also because this backbone should consist of the largest and least tortuous pores in the accessible cluster, it is reasonable to assume that the entire backbone cluster is filled with liquid. Thus, incomplete filling was not expected to affect transport, so $\varnothing_c = 0.169$ was considered as a reliable result for the transport model.

The primary strength of the transport model is that it does not require explicit use of a tortuosity "fudge factor" for description of diffusion through porous systems. This tortuosity instead implicitly governs the values of $\varnothing^E$ and $\varnothing_c$ through the matrix coordination number (z). The higher the value of z, the more complicated the system, and thus the more tortuous the pore structure. The pore space used in transport appeared to successfully follow a tetrakaidecahedral lattice approximation ($z = 14$).

The scaling law for $\varnothing^E$, using the conductivity exponent $\mu = 2.0$, adequately represented the relationship between $\varnothing^E$ and $\varnothing$ up to a total porosity of about 35%. Deviations from the $\varnothing^E$ model at higher $\varnothing$ were thought to occur as individual pores became less important in their contributions to transport and the scaling law became invalid. Transport should accelerate with increasing $\varnothing$ because the tortuosity of each individual pore will decrease as $\varnothing$ becomes larger and the pores begin to merge. Control of small molecule transport, as would be required for manipulation of drug release, thus appeared to be possible only for $\varnothing$ in the approximate range $\varnothing_c < \varnothing \leq 0.35$ as suggested by the fit of the scaling law.

The scaling law for $\varnothing^A$ predicted a value of $\varnothing_c = 0.128$ based on the experimental values of $\varnothing^A$ and $\varnothing$, instead of the expected site percolation threshold of 0.17 for a tetrakaidecahedral lattice. Since helium penetrates each alumina disk from all surfaces in a pycnometry experiment, it is not possible to discriminate actual sample spanning clusters (those that would contribute to transport across the disk as in the $\varnothing^E$ study) from the total accessible volume fraction. While it is still the case that the discontinuities in $\varnothing^I$ and $\varnothing^A$ may be interpreted as occurring at $\varnothing = \varnothing_c$ as in the standard model, the value of $\varnothing_c$ obtained through pycnometry only reflects the point above which $\varnothing^I$ begins decreasing at the expense of total accessible volume fraction and does not necessarily indicate the onset of sample-spanning cluster growth.

The offset in $\varnothing_c$ from the infinite case *appeared* to take on the properties of a finite-size effect such as described by Sahimi (26), i.e., $\varnothing_c(\infty) - \varnothing_c(L) \propto L^{-1/\nu}$, where $\varnothing_c(\infty)$ is the percolation threshold of the infinite lattice, $\varnothing_c(L)$ is the threshold of the finite system, L is the system length, and í is the correlation length exponent defined in Eq. (9); however, since helium can penetrate the disk from any direction and move toward the center with equal probability during the pycnometry experiment, it is equally likely that this offset would occur for systems of infinite and finite L.

Based on these results, the conclusion can be made that a volume exclusion approach such as helium pycnometry may not be an appropriate means of estimating the accessible (i.e., sample-spanning) volume fraction as it cannot identify the onset of the first sample-spanning cluster and thus underestimates $\varnothing_c$. It would be useful, nonetheless, to define the value of $\varnothing_c$ obtained through the $\varnothing^A$ fit as a "critical isolated volume fraction" since it identifies the onset of exponential accessible cluster growth independent of other system information (such as the system length). However, this result must be complemented by additional information regarding backbone cluster properties that can only be obtained through conductivity, transport, or perhaps permeability studies.

Results of the finite-size scaling manipulation of $\varnothing^E$ showed that the transport rate of ionized benzoic acid could be increased by redistributing and consolidating the void space in a disk without significantly affecting the total porosity. This may be a useful means of manipulating the release rate of a ceramic device while simultaneously taking advantage of the added strength imparted by low total

porosity. It appeared that an exponential relationship existed between the quantity $(\varnothing - \varnothing_c)L^{1/\nu}$ and the value $\varnothing^E L^{\mu/\nu}$, in the case of the tetrakaidecahedral alumina matrix, with $\varnothing^E L^{\mu/\nu}$ increasing in magnitude with increasing L.

CONCLUSION

Aqueous transport of a small molecule through alumina disks with total porosities near the critical percolation threshold may be described using a tetrakaidecahedral lattice model. Both transport-dependent and structural properties of the lattice can be obtained using percolation theory scaling relationships, with the transport-dependent data obtained through membrane diffusivity studies offering a better reflection of percolation properties than structural data obtained by helium pycnometry. Redistribution of the pore volume from many small pores into a few large pores, without altering the random distribution of the pore space, may be an effective means of increasing the release rate of a small molecule without increasing total porosity or sacrificing mechanical strength. The use of helium pycnometry may be limited to description of the onset of exponential cluster growth rather than the characterization of sample-spanning clusters. Finite-size scaling can be used to model the impact of pore volume redistribution on transport rate at or below the percolation threshold.

Notations

P(x)	Probability of a site or bond *x* being present in the lattice
z	Coordination number
$\varnothing_c$	Critical percolation threshold
$\varnothing$	Total porosity (total void fraction)
ν	Correlation length exponent (=0.9 in three dimensions)
$\varnothing^A$	Accessible volume fraction (structural property)
β	Accessible lattice exponent (=0.4 in three dimensions)
$\varnothing^I$	Isolated volume fraction (structural property)
$\varnothing^B$	Backbone volume fraction (structural property)
$\varnothing^D$	Dead-end volume fraction (structural property)
γ_B	Backbone lattice exponent (=0.9 in three dimensions)
$\varnothing^E$	Effective diffusivity (transport-dependent property)
μ	Effective conductivity exponent (=2.0 in three dimensions)
D_B	Bulk diffusivity
D_{aq}	Aqueous diffusivity
ρ	Density
c	Concentration of ionized benzoic acid
L	System length in number of voids
t	Time
$\varnothing^S$	Surface volume fraction (structural property)

ACKNOWLEDGMENT

This work was funded in part through a 2-year Advanced Predoctoral Fellowship awarded by the Pharmaceutical Manufacturer's Association Foundation, Washington, DC.

REFERENCES

1. S. R. Ellis. *Porous Alumina Ceramics in Drug Delivery: Processing Concerns and Percolation Models*, Ph.D. Thesis. University of Wisconsin–Madison (1990).
2. D. Stauffer. *Introduction to Percolation Theory*, Taylor & Francis, London, 1985.
3. W. D. Kingery, H. K. Bowen and D. R. Uhlmann. *Introduction to Ceramics,* 2nd ed. Wiley, New York, 1976.
4. E. L. Cussler. *Diffusion: Mass Transport in Fluid Systems*, Cambridge University Press, New York, 1986.
5. G. R. Jerauld, L. E. Scriven, and H. T. Davis. Percolation and conduction on the 3D Voronoi and regular networks: a second case study in topological disorder. *J. Phys. C. Solid State Phys.* **17**(19):3429–3439 (1984).
6. R. B. Pandey, D. Stauffer, A. Margolina, and J. G. Zabolitzky. Diffusion on random systems above, below, and at their percolation threshold in two and three dimensions. *J. Stat. Phys.* **34**(3/4):427–449 (1984).
7. M. Sahimi, B. D. Hughes, L. E. Scriven, and H. T. Davis. Critical exponent of percolation conductivity by finite-size scaling. *J. Phys. C. Solid State Phys.* **16**:L521–L527 (1983).
8. A. B. Shelekhin, A. G. Dixon, and Y. H. Ma. Adsorption, diffusion, and permeation of gases in microporous membranes: III. Application of percolation theory to interpretation of porosity, tortuosity, and surface area in microporous glass membranes. *J. Membr. Sci.* **83**(2):181–198 (1993).
9. S. W. Tam and V. Ambrose. Tritium transport in lithium ceramics porous media. *J. Nucl. Mater.* **191**–**194**:253–257 (1992).
10. R. L. Jerzewski, and N. G. Lordi, Water vapor diffusion in model tablet systems: II. Experiments with lactose anhydrous based tablets. *Int. J. Pharm.* **101**(1–2):45–56 (1994).
11. I. Caraballo, M. Millan, A. Fini, L. Rodriguez, and C. Cavallari. Percolation thresholds in ultrasound compacted tablets. *J. Control Release* **69**:345–355 (2000).
12. A. F. Rime, D. Massuelle, F. Kubel, H. R. Hagemann, and E. Doelker. Compressibility and compactibility of powdered polymers: poly(vinyl chloride) powders. *Eur. J. Pharm. Biopharm.* **44**:315–322 (1997).
13. H. Leuenberger and L. Ineichen. Percolation theory and physics of compression. *Eur. J. Pharm. Biopharm.* **44**:269–272 (1997).
14. D. Blattner, M. Kolb, and H. Leuenberger. Percolation theory and compactibility of binary powder systems. *Pharm. Res.* **7**(2): 113–117 (1990).
15. H. Leuenberger. New trends in the production of pharmaceutical granules: the classical batch concept and the problem of scale-up. *Eur. J. Pharm. Biopharm.* **52**:279–288 (2001).
16. I. Caraballo, M. Fernandez-Arevalo, M. A. Holgado, and A. M. Rabasco. Percolation theory: application to the study of the release behaviour from inert matrix systems. *Int. J. Pharm.* **96**:175–181 (1993).
17. J. E. Hastedt and J. L. Wright. Diffusion in porous materials above the percolation threshold. *Pharm. Res.* **7**(9):893–901 (1990).
18. J. E. Hastedt. *Diffusional Release from a Porous Polymeric Matrix: A Model Based on Per*colation Theory. Ph.D. Thesis. University of Wisconsin–Madison (1990).
19. E. Ryshkewitch and D. W. Richerson. *Oxide Ceramics* (2) Academic, Orlando, FL, (1985).
20. A. Coniglio. Cluster structure near the percolation threshold. *J. Phys. A.* **15**(12):3829–3844 (1982).
21. R. J. Davey and B. Dobbs. On the morphology of ceramic powders. *Chem. Eng. Sci.* **42**(4):631–637 (1987).
22. K. Kendall. Influence of powder structure on processing and properties of advanced ceramics. *Powder Technol.* **58**:151–161 (1989).
23. R. W. Rice. Ceramic processing: an overview. *AIChE J.* **36**(4): 481–510 (1990).
24. K. A. Berry and M. P. Harmer. Effect of MgO solute on microstructure development in Al_2O_3. *J. Am. Ceram. Soc.* **69**(2): 143–148 (1986).
25. N. J. Shaw and R. J. Brook. Structure and grain coarsening during the sintering of alumina. *J. Am. Ceram. Soc.* **69**(2): 107–110 (1986).

26. M. Sahimi. *Applications of Percolation Theory*, Taylor & Francis, London, 1980.
27. M. Yanuka. The mixed bond-site percolation problem and its application to capillary phenomena in porous media. *J. Colloid Interface Sci.* **134**(1):198–205 (1990).
28. K. K. Mohanty, J. M. Ottino, and H. T. Davis. Reaction and transport in disordered composite media: Introduction of percolation concepts. *Chem. Eng. Sci.* **37**(6):905–924 (1982).
29. S. Reyes and K. F. Jensen. Estimation of effective transport coefficients in porous solids based on percolation concepts. *Chem. Eng. Sci.* **40**(9):1723–1734 (1985).
30. S. Havlin, D. Ben-Avaraham, and H. Sompolinsky. Scaling behavior of diffusion on percolation clusters. *Phys. Rev. A.* **27**(3):1730–1733 (1983).
31. S.-I. Lee, Y. Song, T. W. Noh, X.-D. Chen, and J. R. Gaines. Experimental observation of nonuniversal behavior of the conductivity exponent for three-dimensional continuum percolation systems. *Phys. Rev. B.* **34**(10):6719–6724 (1986).
32. F. Brouers and A. Ramsamugh. Relation between conductivity and fluid flow permeability in porous alumina ceramics. *Solid State Commun.* **60**(12):951–953 (1986).
33. F. Brouers and A. Ramsamugh. Percolation and anomalous conduction on fractals in fluid-saturated porous media. *J. Phys. C Solid State Phys.* **21**(9):1839–1847 (1988).
34. A. Margolina, H. Nakanishi, D. Stauffer, and H. E. Stanley. Monte Carlo and series study of corrections to scaling in two-dimensional percolation. *J. Phys. A.* **17**(8):1683–1701 (1984).
35. R. D. Skwierczynski, Characterization of Porous Hydroxyapatite and β-*Whitlockite Ceramic Disks: An Application of Percolation Theory*, M.S. Thesis, University of Wisconsin–Madison (1990).
36. J. W. Boretos. Bioceramics, *Chem. Tech.* April: 224–231 (1987).
37. P. Griss and G. Heimke. Biocompatibility of high density alumina and its application in orthopedic surgery. In D. F. Williams (ed.), *Biocompatibility of Clinical Implant Materials,* CRC Press, Boca Raton, Florida, 1981.
38. Y. W. Chien. *Novel Drug Delivery Systems*, Marcel Dekker, New York, 1982.
39. B. Wickliffe and D. N. Entrekin. Relation of pH to preservative effectiveness II. *J. Pharm. Sci.* **53**(7):769–773 (1964).
40. W. I. Higuchi, S. Prakongpan, and F. Young. Mechanisms of dissolution of human cholesterol gallstones. *J. Pharm. Sci.* **62** (6): 945–948 (1973).